Turbulent Convective Lengthscale in Planetary Cores

Céline Guervilly*[,1], Philippe Cardin[2], and Nathanaël Schaeffer[2]

[1] *School of Mathematics, Statistics and Physics, Newcastle University, Newcastle upon Tyne, NE17RU, UK*

[2] *Univ. Grenoble Alpes, Univ. Savoie Mont Blanc, CNRS, IRD, IFSTTAR, ISTerre, 38000 Grenoble, France*

June 20, 2019

Convection is a fundamental physical process in the fluid cores of planets because it is the primary transport mechanism for heat and chemical species and the primary energy source for planetary magnetic fields. Key properties of convection, such as the characteristic flow velocity and lengthscale, are poorly quantified in planetary cores due to their strong dependence on planetary rotation, buoyancy driving and magnetic fields, which are all difficult to model under realistic conditions. In the absence of strong magnetic fields, the core convective flows are expected to be in a regime of rapidly-rotating turbulence,[1] which remains largely unexplored to date. Here we use a combination of non-magnetic numerical models designed to explore this regime to show that the turbulent convective lengthscale becomes independent of the viscosity and is entirely determined by the flow velocity and planetary rotation. The velocity decreases very rapidly at smaller scales, so this turbulent scale is essentially a lower limit for the energy-carrying lengthscales in the flow. For the first time, we are able to model realistically the dynamics of small non-magnetic cores such as the Moon. Although larger planetary core conditions remain presently out of reach, the independence of the results on the viscosity allows a reliable extrapolation to these objects. For Earth's core conditions, we find that the turbulent scale in the absence of magnetic fields would be approximately 30 km, which is orders of magnitude larger than the 10-m viscous lengthscale. The necessity to resolve the numerically inaccessible viscous scale could therefore be relaxed in future geodynamo simulations pushing towards realistic conditions, at least in weakly-magnetised regions.

The very low fluid viscosity in liquid cores implies that the convective flows are turbulent, but this turbulence differs from both 3D turbulence due to the anisotropy imposed by the rapid planetary rotation and 2D turbulence due to the presence of Rossby waves.[2] Conditions in planetary cores correspond to small Ekman numbers ($Ek = \nu/\Omega R^2$ with viscosity ν, rotation rate Ω and core radius R), large Reynolds numbers ($Re = \mathcal{U}R/\nu$ with flow speed $\mathcal{U}$), and small Rossby numbers ($Ro = \mathcal{U}/\Omega R = ReEk$), with, for instance, $Ek \approx 10^{-15}$, $Re \approx 10^9$ and $Ro \approx 10^{-6}$ in the Earth's core.[3] Numerical models must employ a fluid viscosity that is orders of magnitude larger than realistic values to keep the range of time and length scales involved in the dynamics manageable, with typically $Ek \geq 10^{-7}$ and $Re \leq 10^4$.[4] Unfortunately this has the undesirable effect that convection properties are still controlled by the viscosity.[5,6] In the viscous regime, convection takes the form of tall and narrow columns aligned with the rotation axis with an azimuthal lengthscale, $\mathcal{L}_\nu$, that depends on the viscosity as $Ek^{1/3}$,[7] and so $\mathcal{L}_\nu \approx$10 m for Earth-like parameter values. When nonlinear effects become important in the rapidly-rotating turbulent regime of large Re and low Ro, the convective lengthscale is expected

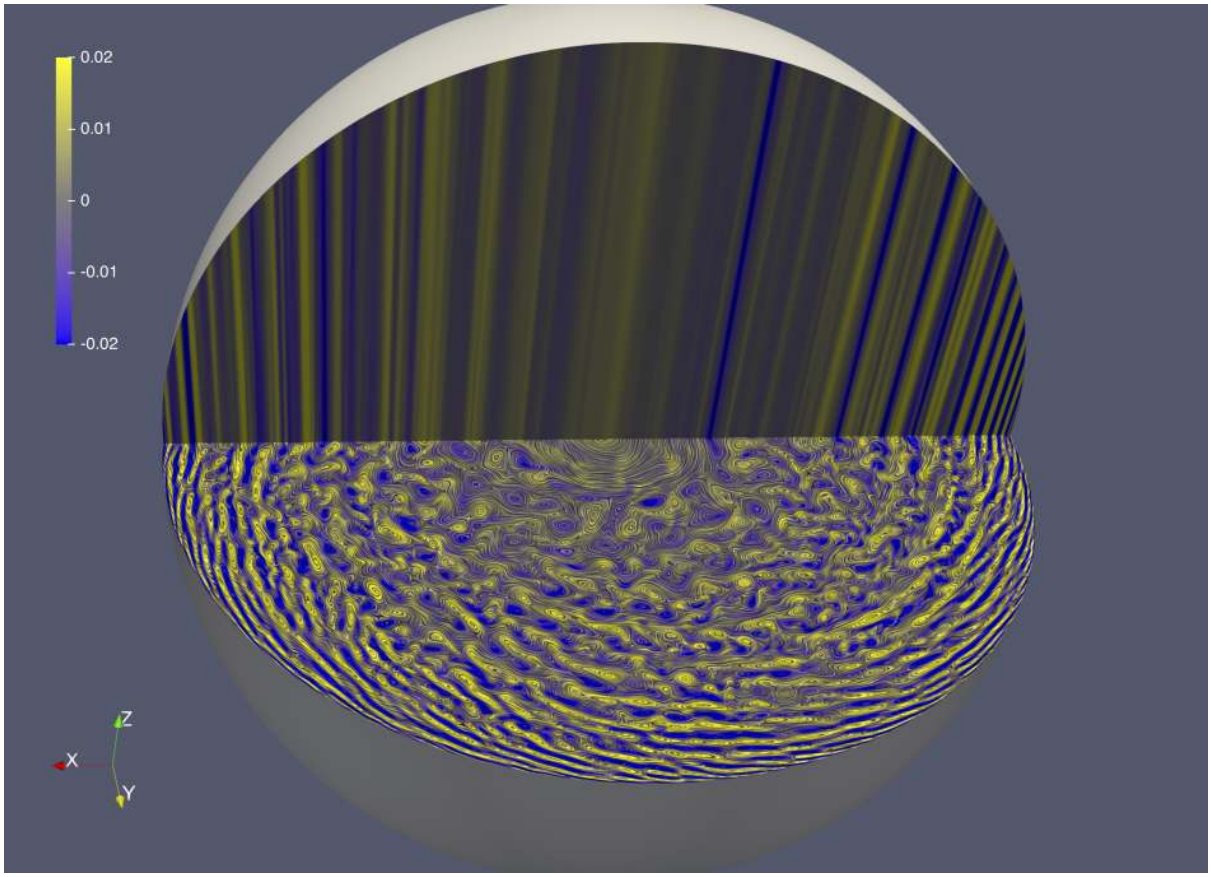

Figure 1: **Flow in the 3D model.** Meridional and equatorial cross-sections of a snapshot of the axial vorticity in the 3D model for $Ek = 10^{-8}$, $Ra = 2 \times 10^{10}$, and $Pr = 10^{-2}$. Streamlines have been superimposed in the equatorial plane. In the colorbar, values of the axial vorticity are normalised by the planetary vorticity 2Ω. The kinetic energy of the velocity projected on a quasi-geostrophic state $(\langle u_s \rangle, \langle u_\phi \rangle, z\beta \langle u_s \rangle)$ (where the angle brackets denote an axial average) is within 0.2% of the total kinetic energy.

to grow above the viscous lengthscale, up to a scale $\mathcal{L}_t$ controlled by the flow velocity.[8–10] The actual value of this turbulent convective lengthscale is currently unknown for planetary cores. The objective of this work is to provide an estimate of $\mathcal{L}_t$ in core conditions using an extensive numerical exploration of the low viscosity regime. We use a combination of a state-of-the-art 3D model[11] down to $Ek = 10^{-8}$ supplemented by a simplified model of quasi-geostrophic (QG) rotating convection[12,13] down to $Ek = 10^{-11}$. The simplified QG model takes advantage of the Proudman-Taylor constraint[14] by assuming that the axial vorticity is invariant along the rotation axis. The QG approximation is well supported by the results of the 3D model shown in Figure 1. The numerical codes solve the governing equations of nonlinear Boussinesq convection driven by homogeneous internal heating in a full sphere geometry (see Methods). Magnetic fields are not included.

For the low Ekman numbers studied here, convection is always in a turbulent state, even near the nonlinear onset,[11,15] and $Re \geq 10^3$. The convection takes the form of vortical plumes that are radially elongated on scales much shorter than the outer radius (Figure 2). At large radius, the steepening of the boundary slope inhibits vortical plume convection.[3] The dynamics there mainly consists of Rossby waves, which appear as elongated vortices with a prograde tilt[16,17] (Figure 2e). Their radial velocities are relatively small so conduction dominates the heat transport in the outer part of the equatorial plane.[18] Hereafter we solely consider the dynamics of the inner convective region, which grows wider with increasing Rayleigh number (Ra,

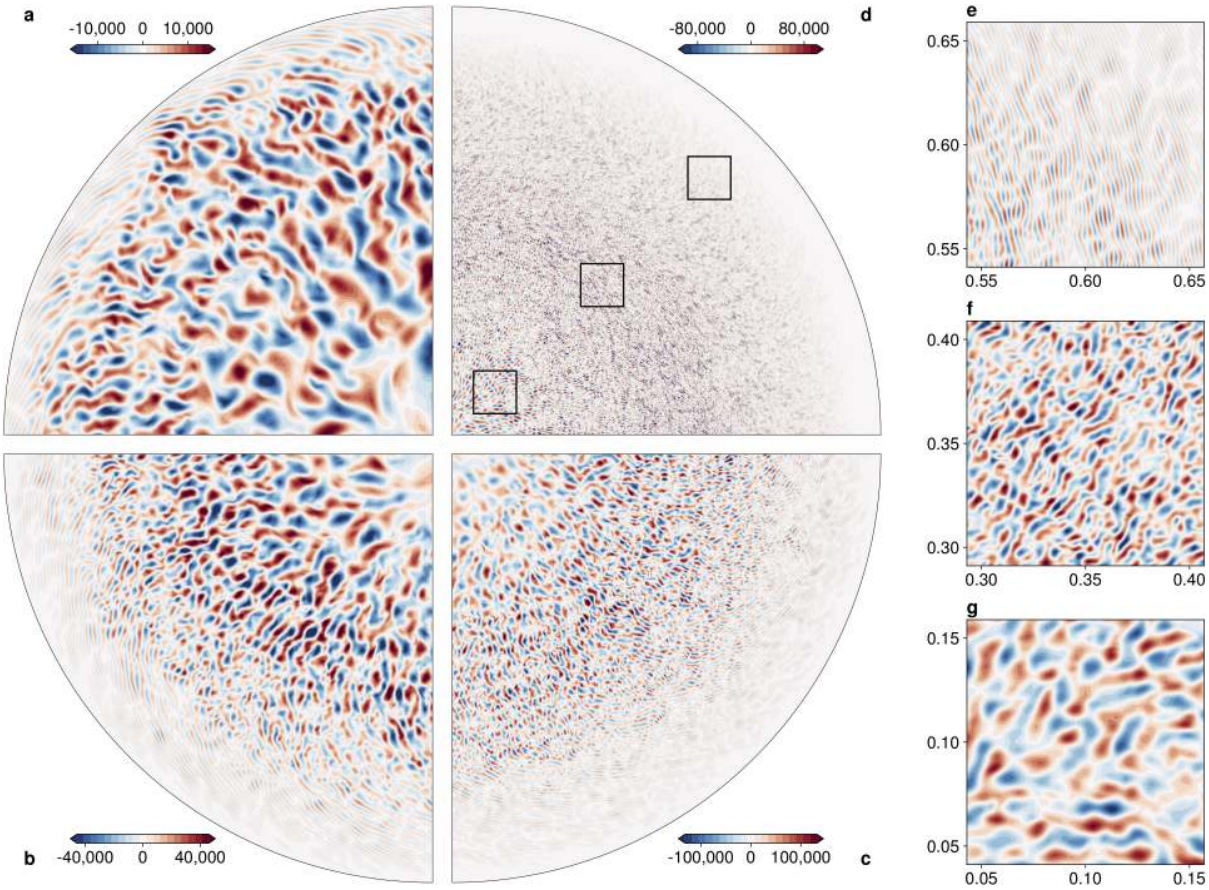

Figure 2: **Effect of the Rossby number on the flow structure.** Snapshots of the radial velocity in a quarter of the equatorial plane during the statistically-steady phase for a) $Ek = 10^{-8}$, $Ra = 2.5 \times 10^{10}$ ($Ro = 6 \times 10^{-5}$), b) $Ek = 10^{-9}$, $Ra = 2.7 \times 10^{11}$ ($Ro = 2 \times 10^{-5}$), c) $Ek = 10^{-10}$, $Ra = 6.3 \times 10^{12}$ ($Ro = 4 \times 10^{-6}$) and d) $Ek = 10^{-11}$, $Ra = 5.25 \times 10^{13}$ ($Ro = 3 \times 10^{-7}$). Case a was performed with the 3D model and cases b-d with the QG model. Close-ups are shown in e-g for the same parameters as in d; e shows the outer conduction-dominated region where the dynamics is dominated by Rossby waves, and f-g the inner convective region. $Pr = 10^{-2}$ in all cases. In the colorbars, values of the radial velocity are normalised by the viscous velocity scale.

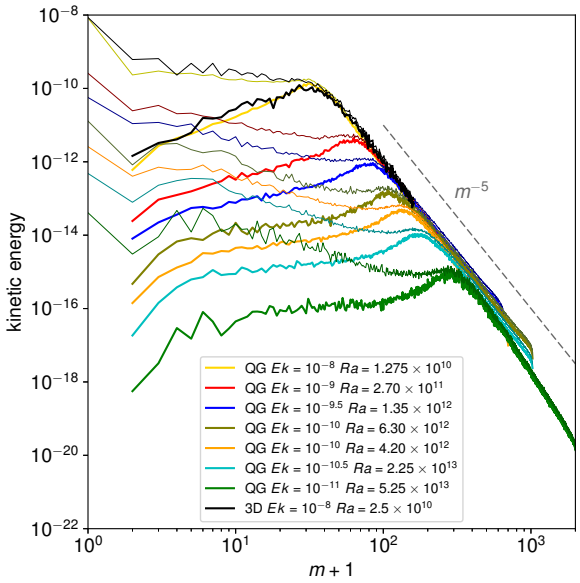

Figure 3: **Distribution of the kinetic energy at different lengthscales.** Power spectra of the total kinetic energy (thin line) and radial kinetic energy (thick line) as a function of the azimuthal wavenumber m at $s = 0.5$ for simulations with different Ekman and Rayleigh numbers for $Pr = 10^{-2}$ performed with the 3D and QG models. The kinetic energy is averaged in time and normalised by $\rho(\Omega R)^2/2$. The lengthscale is inversely proportional to m.

which controls the buoyancy driving). The lengthscale of the convective flows decreases notably with increasing radius (Figures 2f-g). We find that the convective lengthscale is controlled by the Rossby number, rather than by any viscous effect. The flows shown in Figures 1 and 2 are snapshots taken once the system has reached a statistically steady state, and are entirely unlike the linear viscous mode at the convection onset, which consists of drifting columns with a narrow azimuthal lengthscale $\mathcal{L}_\nu$.[7,19] The convective lengthscale increases with the buoyancy driving as seen on the power spectra of the total and radial kinetic energies in Figure 3. The peak of the radial kinetic energy moves to smaller azimuthal wavenumber m for increasing Ra, as can be observed for the two different Rayleigh numbers shown at $Ek = 10^{-10}$, and is located at significantly smaller wavenumber ($m = 133$ and 106 for the smaller and larger Ra) than the wavenumber of the marginal linear viscous mode at onset ($m = 258$). Remarkably, the spectra at different Ek and Ra superpose well at wavenumbers larger than the peak, and follow a steep slope m^{-5}.[20] There is therefore a well-defined characteristic convective lengthscale that carries most of the radial kinetic energy, and below this scale, the velocity amplitude drops very rapidly. This characteristic lengthscale is thus a limit below which only weak convective motions occur, thereby drastically restricting viscous control and dissipation in the bulk. At wavenumbers smaller than the peak, the velocity becomes anisotropic with a dominant azimuthal component. The kinetic energy is transferred to larger scales, where the dynamics is dominated by propagating Rossby waves, and viscous dissipation occurs in the boundary layers.

In the rapidly-rotating turbulent regime, the increase of the convective lengthscale with the buoyancy driving is expected from scaling arguments,[8–10] which assume that the production of axial vorticity is governed by a triple inviscid balance between vortex stretching, advection and buoyancy (the so-called Coriolis-Inertia-Archimedes balance). The scaling gives a convective lengthscale that depends on the flow velocity as $\mathcal{L}_t \sim (Ro/|\beta|)^{1/2}$, where β is a geometrical factor related to the boundary slope (see Methods). This lengthscale is consistent with the -5 slope observed on the power spectra of the kinetic energy. Assuming that the transport in the fluid bulk controls the heat transfer,[21] the scaling uses a balance between the nonlinear advection of

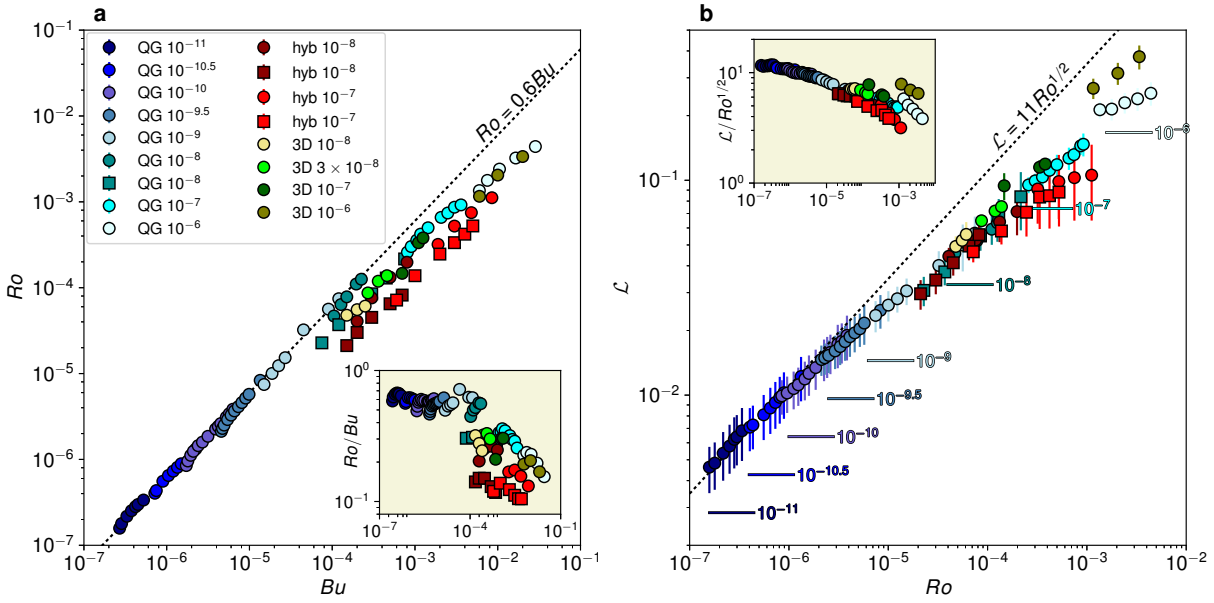

Figure 4: **Scaling of the velocity and lengthscale.** a) Rossby number Ro as a function of the buoyancy parameter Bu and b) convective lengthscale $\mathcal{L}$ as a function of Ro in 3D (green points), QG (blue), and hybrid (red) simulations. Marker colours correspond to Ek (values given in the legend) and shapes to Pr (circles: $Pr = 10^{-2}$; squares: $Pr = 10^{-1}$). In b, $\mathcal{L}$ is radially averaged between $s \in [0.1, 0.6]$; the vertical bars give the standard deviation in this interval. The horizontal lines give the linear viscous lengthscale $\mathcal{L}_\nu$ at $s = 0.5$ for a given Ek and $Pr = 10^{-2}$. The insets show the data compensated by the theoretical scaling as a function of a) Bu and b) Ro.

temperature and the transport of the mean temperature background to obtain $Re \sim RaEk/Pr$, or simply $Ro \sim Bu$ with the viscosity-free buoyancy parameter $Bu = RaEk^2/Pr$. The Prandtl number, Pr, is the ratio of viscosity to thermal diffusivity and is expected to be $0.01 - 0.1$ in liquid metal cores. The theoretical scaling law is tested in Figure 4 against results obtained with the 3D and QG models and published results obtained with a hybrid model that uses the QG approximation coupled to the 3D temperature.[18] The characteristic convective lengthscale $\mathcal{L}$ corresponds to the peak of the radial kinetic energy spectra. Points obtained at different Ek collapse onto a single curve, especially for $Ek < 10^{-9}$, showing that the dependence of the results on the viscosity becomes negligible when core conditions are approached. Importantly, the good agreement obtained between the different numerical models supports the use of the QG approximation for modelling rapidly-rotating convection. The data of the velocity and lengthscale compensated by their respective theoretical scaling laws align on a plateau at small Ek, and thus indicate that the agreement between the simulations and the theoretical scaling improves progressively as Ek decreases. The lengthscales show little dependence on Pr; for the velocity scaling, the slope is unaffected by Pr but cases with larger Pr tend to have slightly smaller prefactor. To avoid the "shingling" effect that occurs when using diffusion-free parameters,[22] the scaling of the Reynolds number is shown in Extended Data Figure 1 and confirms the overlap of the data for $Ek \leq 10^{-9}$ and the good agreement with the exponent predicted by the theoretical scaling. While the lengthscale $\mathcal{L}$ corresponds to an azimuthal size in Figure 4, we confirm that the radial lengthscale obtained from radial correlations is in good agreement with this azimuthal scale in Extended Data Figure 2. The radial dependence of the lengthscale observed in Figure 2 is also in agreement with the theoretical dependence on $|\beta|^{-1/2}$ as shown in the Extended Data Figure 3. Additional QG simulations performed with differential heating in the presence of an inner core (see Methods) show that the scaling law $\mathcal{L}(Ro)$ of Figure 4 is

valid for other heating modes (Extended Data Figure 4).

The smallest Ekman number computed with our simplified QG numerical model, $Ek = 10^{-11}$, is approximately the value for the core of the Moon.[23] Non-magnetic convection in the lunar core is bracketed between the extinction of the dynamo, which occurs at $Re \approx 10^7$ corresponding to a critical magnetic Reynolds number of 10[24] and the cessation of nonlinear convection, which occurs at $Re \approx 10^3$.[11,15] Between these two events, our results predict that the turbulent lengthscale decreases as $Ro^{1/2} \sim Ra^{1/2}$ from $0.1R \approx 10$km to $0.001R \approx 0.1$km, implying a large reduction of the heat transport efficiency (see Methods).

Whilst being non-magnetic, our study has interesting implications for the Earth's core dynamics and geodynamo modelling. Characteristic flow speeds at the core-mantle boundary inferred from the geomagnetic secular variation have $Ro \approx 10^{-6}$,[25] which corresponds to $\mathcal{L}_t \approx 0.01R \approx 30$km. This value is close to the magnetostrophic cross-over scale,[26] a theoretical scale below which magnetic forces become dynamically important and estimated to be 1-100km in the Earth's core. The geomagnetic field therefore likely affects core convection. In the presence of magnetic fields, the convective lengthscale is expected to increase,[27,28] so the 30-km scale will likely remain a lower limit for the energy-carrying lengthscales. In the most recent geodynamo simulations,[28–30] the magnetic field is heterogeneous with a strong dynamical influence in some regions, but not in others. The convection is thus multi-scale, and the dynamics exhibits a viscous dependence ($\mathcal{L}_\nu \sim Ek^{1/3}$) in the weakly-magnetised regions. For more realistic turbulent conditions, we propose that these regions would be in Coriolis-Inertia-Archimedes balance instead of viscous balance. This dynamical shift opens a promising new route for more realistic planetary core simulations because the large increase in the characteristic flow lengthscale from $\mathcal{L}_\nu$ to $\mathcal{L}_t$ and the steepness of the kinetic energy spectra beyond $\mathcal{L}_t$ permit a relaxation of the numerical resolution constraint in the bulk.

References

[1] Aurnou, J. *et al.* Rotating convective turbulence in Earth and planetary cores. *Phys. Earth Planet. Int.* **246**, 52–71 (2015).

[2] Vallis, G. K. *Atmospheric and oceanic fluid dynamics: fundamentals and large-scale circulation* (Cambridge University Press, 2006).

[3] Jones, C. A. Thermal and compositional convection in the outer core. In *Treatise on Geophysics 2nd ed.*, 115 – 159 (Elsevier, 2015).

[4] Gastine, T., Wicht, J. & Aubert, J. Scaling regimes in spherical shell rotating convection. *J. Fluid Mech.* **808**, 690–732 (2016).

[5] King, E. & Buffett, B. Flow speeds and length scales in geodynamo models: The role of viscosity. *Earth Planet. Sci. Lett.* **371**, 156–162 (2013).

[6] Oruba, L. & Dormy, E. Predictive scaling laws for spherical rotating dynamos. *Geophys. J. Int.* **198**, 828–847 (2014).

[7] Jones, C. A., Soward, A. M. & Mussa, A. I. The onset of thermal convection in a rapidly rotating sphere. *J. Fluid Mech.* **405**, 157–179 (2000).

[8] Stevenson, D. J. Turbulent thermal convection in the presence of rotation and a magnetic field: a heuristic theory. *Geophys. Astrophys. Fluid Dyn.* **12**, 139–169 (1979).

[9] Ingersoll, A. P. & Pollard, D. Motion in the interiors and atmospheres of Jupiter and Saturn - Scale analysis, anelastic equations, barotropic stability criterion. *Icarus* **52**, 62–80 (1982).

[10] Aubert, J., Brito, D., Nataf, H.-C., Cardin, P. & Masson, J.-P. A systematic experimental study of rapidly rotating spherical convection in water and liquid gallium. *Phys. Earth Planet. Int.* **128**, 51–74 (2001).

[11] Kaplan, E. J., Schaeffer, N., Vidal, J. & Cardin, P. Subcritical thermal convection of liquid metals in a rapidly rotating sphere. *Phys. Rev. Lett.* **119**, 094501 (2017).

[12] Or, A. C. & Busse, F. H. Convection in a rotating cylindrical annulus. II. Transitions to asymmetric and vacillating flow. *J. Fluid Mech.* **174**, 313–326 (1987).

[13] Gillet, N., Brito, D., Jault, D. & Nataf, H.-C. Experimental and numerical study of convection in a rapidly rotating spherical shell. *J. Fluid Mech.* **580**, 83–121 (2007).

[14] Taylor, G. I. The motion of a sphere in a rotating liquid. *Proc. R. Soc. Lond. A* **102**, 180–189 (1922).

[15] Guervilly, C. & Cardin, P. Subcritical convection of liquid metals in a rotating sphere using a quasi-geostrophic model. *J. Fluid Mech.* **808**, 61–89 (2016).

[16] Miyagoshi, T., Kageyama, A. & Sato, T. Zonal flow formation in the Earth's core. *Nature* **463**, 793–796 (2010).

[17] Sumita, I. & Olson, P. Experiments on highly supercritical thermal convection in a rapidly rotating hemispherical shell. *J. Fluid Mech.* **492**, 271–287 (2003).

[18] Guervilly, C. & Cardin, P. Multiple zonal jets and convective heat transport barriers in a quasi-geostrophic model of planetary cores. *Geophys. J. Int.* **211**, 455–471 (2017).

[19] Zhang, K. Spiralling columnar convection in rapidly rotating spherical fluid shells. *J. Fluid Mech.* **236**, 535–556 (1992).

[20] Schaeffer, N. & Cardin, P. Rossby-wave turbulence in a rapidly rotating sphere. *Nonlinear Process. Geophys.* **12**, 947–953 (2005).

[21] Julien, K., Knobloch, E., Rubio, A. & Vasil, G. Heat Transport in Low-Rossby-Number Rayleigh-Bénard Convection. *Phys. Rev. Lett.* **109**, 254503 (2012).

[22] Cheng, J. S. & Aurnou, J. M. Tests of diffusion-free scaling behaviors in numerical dynamo datasets. *Earth Planet. Sci. Lett.* **436**, 121–129 (2016).

[23] Weber, R. C., Lin, P.-Y., Garnero, E. J., Williams, Q. & Lognonne, P. Seismic detection of the lunar core. *Science* **331**, 309–312 (2011).

[24] Christensen, U. R. & Aubert, J. Scaling properties of convection-driven dynamos in rotating spherical shells and application to planetary magnetic fields. *Geophy. J. Int.* **166**, 97–114 (2006).

[25] Holme, R. & Olsen, N. Core surface flow modelling from high-resolution secular variation. *Geophys. J. Int.* **166**, 518–528 (2006).

[26] Aurnou, J. & King, E. The cross-over to magnetostrophic convection in planetary dynamo systems. *Proc. R. Soc. A* **473**, 20160731 (2017).

[27] Chandrasekhar, S. *Hydrodynamic and hydromagnetic stability* (Clarendon, Oxford, 1961).

[28] Yadav, R., Gastine, T., Christensen, U., Wolk, S. J. & Poppenhaeger, K. Approaching a realistic force balance in geodynamo simulations. *Proc. Natl. Acad. Sci.* **113**, 12065–12070 (2016).

[29] Aubert, J., Gastine, T. & Fournier, A. Spherical convective dynamos in the rapidly rotating asymptotic regime. *J. Fluid Mech.* **813**, 558–593 (2017).

[30] Schaeffer, N., Jault, D., Nataf, H.-C. & Fournier, A. Turbulent geodynamo simulations: a leap towards Earth's core. *Geophys. J. Int.* **211**, 1–29 (2017).

Acknowledgements

C.G. was supported by the UK Natural Environment Research Council under grant NE/M017893/1. P.C. and N.S. were supported by the French *Agence Nationale de la Recherche* under grants ANR-13-BS06-0010 (TuDy) and ANR-14-CE33-0012 (MagLune). N.S. acknowledges GENCI for access to resource Occigen (CINES) under grant A0020407382 and A0040407382. This research made use of the Rocket High Performance Computing service at Newcastle University, the ARCHER UK National Supercomputing Service (http://www.archer.ac.uk), and the DiRAC@Durham facility managed by the Institute for Computational Cosmology on behalf of the STFC DiRAC HPC Facility (www.dirac.ac.uk) and funded by BEIS capital funding via STFC capital grants ST/P002293/1, ST/R002371/1 and ST/S002502/1, Durham University and STFC operations grant ST/R000832/1. Parts of the computations were also performed on the Froggy platform of CIMENT (https://ciment.ujf-grenoble.fr), supported by the Rhône-Alpes region (CPER07_13 CIRA), OSUG@2020 LabEx (ANR10 LABX56) and Equip@Meso (ANR10 EQPX-29-01). ISTerre is part of Labex OSUG@2020 (ANR10 LABX56). This is a post-peer-review, pre-copyedit version of an article published in Nature. The final authenticated version is available online at: http://dx.doi.org/10.1038/s41586-019-1301-5.

Author contributions

C.G. and P.C. performed the numerical simulations with the QG code. N.S. performed the numerical simulations with the 3D code. All authors contributed to the analysis of the data and the preparation of the manuscript.

Competing interests

The authors declare no competing interests.

Additional information

Reprints and permissions information is available at www.nature.com/reprints. Correspondence and requests for materials should be addressed to celine.guervilly@ncl.ac.uk.

Methods

We model Boussinesq convection driven by homogeneous internal heating in a full sphere geometry. This problem is relevant for planetary cores without a solid inner core, and thus, for most of the Earth's history.[31] The model does not include magnetic fields. The sphere rotates at the rate Ω around the axis directed along $\boldsymbol{e}_z$. The acceleration due to gravity is radial and increases linearly, $\boldsymbol{g} = -g_0 r \boldsymbol{e}_r$. The governing equations are written in dimensionless form, obtained by scaling lengths with the outer radius R, times with R^2/ν where ν is the fluid kinematic viscosity, and temperature with $\nu S R^2/(6\rho C_p \kappa^2)$, where S is the internal volumetric heating, κ the thermal diffusivity, ρ the density, and C_p the heat capacity at constant pressure. The dimensionless numbers are: the Ekman number, $Ek = \nu/(\Omega R^2)$, the Rayleigh number, $Ra = \alpha g_0 S R^6/(6\rho C_p \nu \kappa^2)$, where α is the thermal expansion coefficient, and the Prandtl number, $Pr = \nu/\kappa$. This study focuses on Prandtl numbers smaller that unity, which are relevant for thermal convection of liquid metal cores.[32] The system of dimensionless equations is:

$$\frac{\partial \mathbf{u}}{\partial t} + (\mathbf{u}\cdot\boldsymbol{\nabla})\,\mathbf{u} + \frac{2}{Ek}\boldsymbol{e}_z \times \mathbf{u} = -\boldsymbol{\nabla} p + \boldsymbol{\nabla}^2 \mathbf{u} + Ra\Theta \mathbf{r}, \tag{1}$$

$$\nabla \cdot \mathbf{u} = 0, \tag{2}$$

$$\frac{\partial \Theta}{\partial t} + \mathbf{u}\cdot\nabla\Theta - \frac{2}{Pr} r u_r = \frac{1}{Pr}\nabla^2\Theta, \tag{3}$$

where $\mathbf{u}$ is the velocity field, p the pressure, and Θ the temperature perturbation relative to the static temperature $T_s = (1-r^2)/Pr$. We use no-slip boundary conditions and fixed temperature at the outer boundary.

3D numerical model

For the 3D simulations, we use the code XSHELLS,[11] which solves Equations (1)-(3) using finite differences in the radial direction and spherical harmonic expansion.[33] The input parameters and numerical resolutions used for the 3D simulations are given in Supplementary Information. In the 3D simulations, the Prandtl number is fixed to $Pr = 10^{-2}$ and the Ekman number is varied between 10^{-6} and 10^{-8}. The most computationally demanding simulations performed at $Ek = 10^{-8}$ were run with a numerical resolution of 2016 radial grid points and truncation degree $L = 351$ and order $M = 319$ for the spherical harmonics. Hyperviscosity was used in all the 3D simulations, with viscosity depending on spherical harmonic degree ℓ, but only for $\ell > 0.9L$.[11] We use $\nu(\ell) = \nu_0$ for $\ell < \ell_c = 0.9L$ and $\nu(\ell) = \nu_0 q^{\ell-\ell_c}$ for $\ell \geq \ell_c$. We set $q = (\nu_{max}/\nu_0)^{1/(L-\ell_c)}$ and $\nu_{max} \leq 100$.

Quasi-geostrophic numerical model

For simulations at smaller Ekman numbers, we assume that the rotational constraint is such that the variations of the velocity along the axial direction are small compared with the variations along the orthogonal directions. We use a quasi-geostrophic (QG) approximation for rapidly-rotating spherical convection developed from the Busse[34] annulus model[12,35] and widely used in the context of planetary core convection.[36–40] The dynamics are assumed to be dominated by the geostrophic balance, i.e. the Coriolis force balances the pressure gradient at leading order. The leading-order velocity $\mathbf{u}_\perp$ is invariant along z and $\mathbf{u}_\perp = (u_s, u_\phi, 0)$ in cylindrical polar coordinates. Quasi-geostrophic convection is driven by the cylindrical component of gravity, $-g_0 s$. By taking the axial average of the z-component of the curl of the Navier-Stokes equation, we obtain the equation for the leading-order axial vorticity, ζ,

$$\frac{\partial \zeta}{\partial t} + (\mathbf{u}_\perp \cdot \boldsymbol{\nabla}_\perp)\,\zeta - \left(\frac{2}{Ek} + \zeta\right)\left\langle \frac{\partial u_z}{\partial z}\right\rangle = \nabla_\perp^2 \zeta - Ra \left\langle \frac{\partial \Theta}{\partial \phi}\right\rangle, \tag{4}$$

where $\boldsymbol{\nabla}_\perp f \equiv (\partial_s f, \partial_\phi f/s, 0)$, $\nabla^2_\perp f \equiv \partial^2_s f + s^{-1}\partial_s f + s^{-2}\partial^2_\phi f$, and the angle brackets denote an axial average between $\pm H$ with $H = \sqrt{1-s^2}$ the height of the spherical boundary from the equatorial plane.

The velocity is described by a streamfunction ψ that models the non-axisymmetric (i.e. ϕ-dependent) components with the addition of an axisymmetric azimuthal flow, $\overline{u_\phi}$, where the overbar denotes an azimuthal average,

$$\mathbf{u}_\perp = \frac{1}{H}\boldsymbol{\nabla} \times (H\psi \boldsymbol{e}_z) + \overline{u_\phi}\boldsymbol{e}_\phi. \tag{5}$$

This choice of the streamfunction accounts for mass conservation at the outer boundary.[41] We assume that the axial velocity u_z is linear in z and has two contributions: the main contribution comes from mass conservation at the outer boundary and is proportional to $\beta = H'/H$; the second contribution is due to Ekman pumping, which is produced by the viscous boundary layer and scales as $Ek^{1/2}$. The Ekman pumping is parametrised by the formula obtained by asymptotic methods in the limit of small Ek for a linear Ekman layer.[42]

The streamfunction ψ only describes the non-axisymmetric motions, so the axisymmetric azimuthal velocity, $\overline{u_\phi}$, is obtained by taking the azimuthal and axial averages of the ϕ-component of the Navier-Stokes equation to give

$$\frac{\partial \overline{u_\phi}}{\partial t} + \overline{u_s \frac{\partial u_\phi}{\partial s}} + \frac{\overline{u_s u_\phi}}{s} = \nabla^2 \overline{u_\phi} - \frac{\overline{u_\phi}}{s^2} - \frac{1}{Ek^{1/2} H^{3/2}} \overline{u_\phi}, \tag{6}$$

where the last term on the right-hand side corresponds to the Coriolis term simplified using mass conservation.[36]

The equation for the temperature perturbation Θ in the quasi-geostrophic model is obtained by taking the axial average of the temperature equation and assuming that Θ is invariant along z to obtain

$$\frac{\partial \Theta}{\partial t} + \mathbf{u} \cdot \boldsymbol{\nabla}_\perp \Theta - \frac{4}{3Pr} s u_s = \frac{1}{Pr} \nabla^2_\perp \Theta. \tag{7}$$

Note that here we use the gradient of the z-averaged static temperature profile, $\langle T_s \rangle' = -4s/(3Pr)$, rather than the gradient of the z-invariant static temperature profile, $(T_s^{2d})' = -3s/Pr$, to allow for a direct comparison of the Rayleigh numbers used in the different models. The assumption that Θ is invariant along z is not rigorously justified and is used for numerical convenience because it permits us to treat the numerical problem in two dimensions, thereby considerably reducing the computational load. The evolution equation for the streamfunction, axisymmetric velocity and temperature are solved on a 2D grid in the equatorial plane. The QG code uses a pseudo-spectral code with a Fourier decomposition in the azimuthal direction and a second-order finite-difference scheme in radius with irregular spacing. The input parameters and the numerical resolutions used for the QG simulations are given in Supplementary Information. The Prandtl number is varied between 10^{-1} and 10^{-2} and the Ekman number is varied between 10^{-6} and 10^{-11}, allowing an overlap with the 3D simulations over 2 decades in Ek. The most computationally demanding simulations performed at $Ek = 10^{-11}$ were run with a numerical resolution of 4000 radial grid points and 2048 Fourier modes in azimuth.

The influence of the assumption of z-invariance of Θ on the QG results is tested by comparing the QG results with published results obtained with a hybrid QG-3D model[18] at $Ek \in [10^{-8}, 10^{-7}]$. In the hybrid model, the temperature is solved in 3D and coupled to the QG implementation for the velocity. Figure 4 shows good agreement obtained between the QG and hybrid results for overlapping parameters, demonstrating that, while this assumption is not mathematically justified, it does not significantly influence QG convection.

Quasi-geostrophic model with differential heating

To test the dependence of our results on the heating mode and the presence of an inner core, we

performed additional QG simulations using differential heating with fixed temperature boundary conditions and an inner core of radius $R_i = 0.35$. The temperature is scaled with $Pr\Delta T$. The equation for the temperature perturbation is solved in 2D with a static temperature gradient $(T_s^{2d})' = \gamma/(Pr\ln(R_i)s)$, where the constant $\gamma = 0.445$ is used to re-scale the z-invariant temperature profile so that it closely corresponds to the z-averaged static temperature profile.[39] This re-scaling allows to compare directly the Rayleigh numbers used in QG simulations with the ones used in 3D models. The Prandtl number is varied between 1 and 10^{-2} and the Ekman number is varied between 10^{-8} and 10^{-10}. The input parameters and the numerical resolutions used for the QG simulations with differential heating are given in Supplementary Information. Extended Data Figure 4 shows that the azimuthal convective lengthscale as a function of the Rossby number for these additional simulations closely follows the scaling law derived for the QG simulations with internal heating and without inner core.

Definition of the output parameters

The simulations are started from either a small temperature perturbation or the snapshot of a previous simulation performed at a different Rayleigh number in order to minimise the transient phase before saturation. All simulations are run to saturation as shown in Extended Data Figure 5, where we plot the time series of the kinetic energy density for one representative QG case at $Ek = 10^{-11}$ and one representative 3D case at $Ek = 10^{-8}$. For consistency, the kinetic energy density is defined in both cases as

$$K = \frac{1}{2V}\int \left(u_s^2 + u_\phi^2\right) dV, \tag{8}$$

where V is the volume of the sphere, and the kinetic energy density of the axisymmetric velocity as

$$\overline{K} = \frac{1}{2V}\int \overline{u_\phi}^2 dV. \tag{9}$$

A number of output parameters are given in Supplementary Information. The characteristic velocity $\mathcal{U}$ used to calculate the Rossby and Reynolds numbers is based on the r.m.s. radial velocity averaged in volume and time over at least 10 convective turnover timescales.

The convective lengthscale is calculated as $\mathcal{L}(s) = \pi s/m_p(s)$, where m_p is the wavenumber at the peak of the radial kinetic energy spectrum. The peak is determined by smoothing the time-averaged radial kinetic energy spectra with a polynomial of degree 14.

The radial lengthscale of the convective flow $\mathcal{L}_r(s)$ is calculated using the auto-correlation function f of the radial component of the velocity field. For a given radius s, we calculate

$$f(ds) = \overline{u_s(s,\phi,t)u_s(s+ds,\phi,t)}, \tag{10}$$

where the overbar denotes an azimuthal average. Snapshots covering at least 2 dynamical timescales are used to compute the temporal average. $\mathcal{L}_r(s)$ is the full width at half maximum of f.

Inviscid scaling theory

The theoretical scaling of the velocity and lengthscale[3,4,8–10] assumes a three-term balance in the axial vorticity equation between the vorticity advection, vortex stretching and vorticity generation by buoyancy:

$$\frac{Re^2}{\mathcal{L}_t^2} \sim \frac{|\beta|Re}{Ek} \sim \frac{Ra\mathcal{T}}{\mathcal{L}_t}, \tag{11}$$

where $\mathcal{T}$ denotes a typical temperature perturbation and we assumed that the typical axial vorticity is $Re/\mathcal{L}_t$. The turbulent lengthscale then scales as $\mathcal{L}_t \sim (Ro/|\beta|)^{1/2}$. Assuming that, in rapidly-rotating convection, the heat transfer is controlled by the transport in the bulk of

the fluid rather than the thermal boundary layers,[21] gives a balance between the nonlinear advection of heat and the transport of the mean temperature background in the temperature equation:[3]

$$\frac{Re\mathcal{T}}{\mathcal{L}_t} \sim \frac{sRe}{Pr}. \tag{12}$$

Combining (11) and (12) leads to $Re \sim RaEk/Pr$, where we neglected the geometric term $s/|\beta|$. The efficiency of the heat transport can be measured by the ratio q/q_s with the convective heat flux $q = Pr\mathcal{T}Re$ and the static heat flux $q_s \sim 1/Pr$ in dimensionless form. The theoretical scalings of the velocity and temperature perturbation imply that $q/q_s \sim \mathcal{L}_t^3(Pr/Ek)$.

References

[31] Labrosse, S. Thermal evolution of the core with a high thermal conductivity. *Phys. Earth Planet. Int.* **247**, 36–55 (2015).

[32] Pozzo, M., Davies, C., Gubbins, D. & Alfe, D. Thermal and electrical conductivity of iron at Earth's core conditions. *Nature* **485**, 355–358 (2012).

[33] Schaeffer, N. Efficient spherical harmonic transforms aimed at pseudospectral numerical simulations. *Geochemistry, Geophysics, Geosystems* **14**, 751–758 (2013).

[34] Busse, F. H. Thermal instabilities in rapidly rotating systems. *J. Fluid Mech.* **44**, 441–460 (1970).

[35] Cardin, P. & Olson, P. Chaotic thermal convection in a rapidly rotating spherical shell: consequences for flow in the outer core. *Phys. Earth Planet. Inter.* **82**, 235–259 (1994).

[36] Aubert, J., Gillet, N. & Cardin, P. Quasigeostrophic models of convection in rotating spherical shells. *Geochemistry Geophysics Geosystems* **4**, 1052 (2003).

[37] Morin, V. & Dormy, E. Time dependent beta-convection in rapidly rotating spherical shells. *Phys. Fluids* **16**, 1603–1609 (2004).

[38] Plaut, E., Lebranchu, Y., Simitev, R. & Busse, F. H. On the Reynolds stresses and mean fields generated by pure waves: Applications to shear flows and convection in a rotating shell. *J. Fluid Mech.* **602**, 303–326 (2008).

[39] Gillet, N. & Jones, C. A. The quasi-geostrophic model for rapidly rotating spherical convection outside the tangent cylinder. *J. Fluid Mech.* **554**, 343–369 (2006).

[40] Calkins, M., Aurnou, J., Eldredge, J. & Julien, K. The influence of fluid properties on the morphology of core turbulence and the geomagnetic field. *Earth Planet. Sci. Lett.* **359**, 55–60 (2012).

[41] Schaeffer, N. & Cardin, P. Quasigeostrophic model of the instabilities of the Stewartson layer in flat and depth-varying containers. *Phys. Fluids* **17**, 104111 (2005).

[42] Greenspan, H. P. *The theory of rotating fluids* (Cambridge University Press, 1968).

Data availability

Source data for figures 3 and 4 are provided with the paper. The synthetic data generated during this study are included in the Supplementary Information file. Any additional data that support the findings of this study are available from the corresponding author on reasonable request.

Code availability

The 3D numerical code XSHELLS is freely available at https://bitbucket.org/nschaeff/xshells and distributed under the open source CeCILL License. The QG numerical code is available from the corresponding author on request.

Extended Data Figure 1: Scaling of the Reynolds number

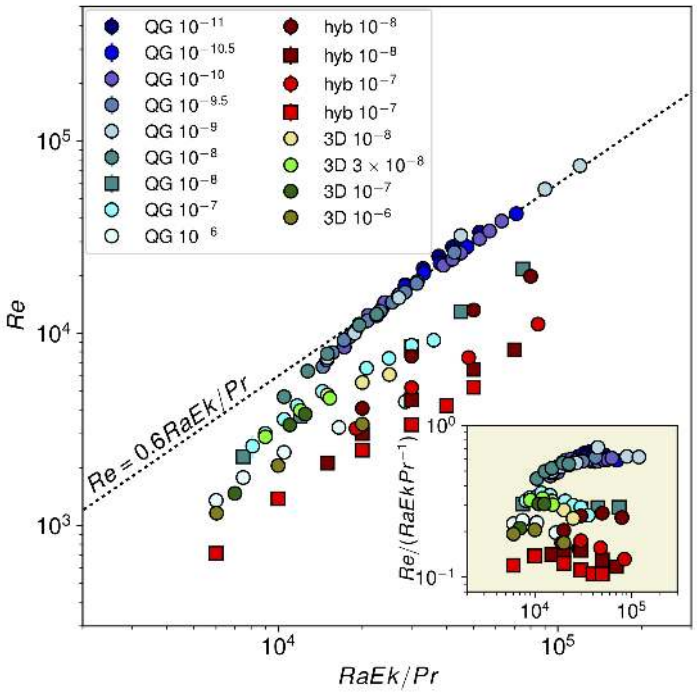

Figure 1: Reynolds number as a function of $RaEk/Pr$ in simulations performed with the 3D model (green points) for $Ek \in [10^{-8}, 10^{-6}]$, the QG model (blue) for $Ek \in [10^{-11}, 10^{-6}]$, and the hybrid model (red) for $Ek \in [10^{-8}, 10^{-7}]$. Marker colours correspond to Ekman numbers (values given in the legend) and marker shapes to Prandtl numbers (circles: $Pr = 10^{-2}$ and squares: $Pr = 10^{-1}$). The inset shows the data compensated by the theoretical scaling as a function of $RaEk/Pr$.

Extended Data Figure 2: Comparison of the radial lengthscale with the azimuthal lengthscale

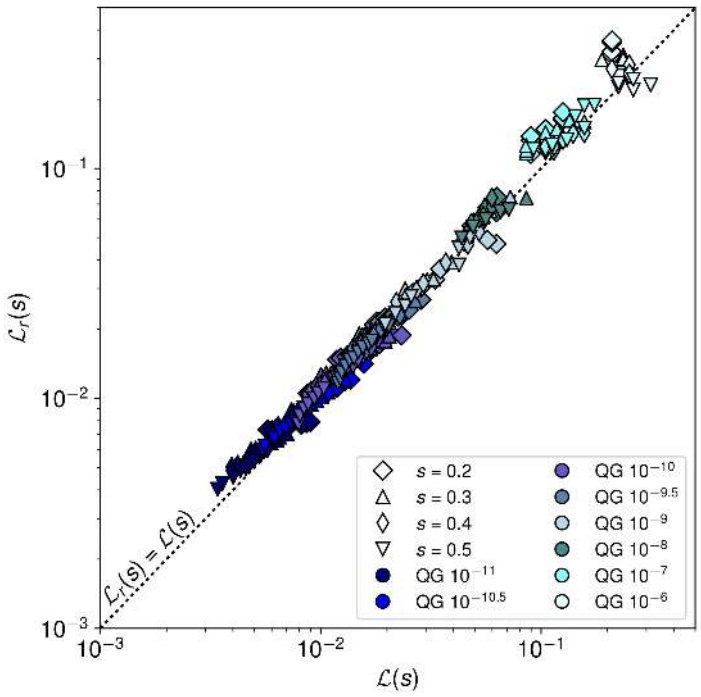

Figure 2: Radial scale of the convective flows $\mathcal{L}_r(s)$ as a function of the azimuthal lengthscale $\mathcal{L}(s)$ obtained with the QG model at different radii. Marker colours correspond to Ekman numbers (with $Pr = 10^{-2}$) and marker shapes to different radii. The radial scale is calculated from auto-correlation functions of the radial velocity. The convective lengthscale corresponds to an azimuthal scale calculated from the peak of the power spectra of the radial kinetic energy at the radius s.

Extended Data Figure 3: Variation of the convective lengthscale with radius

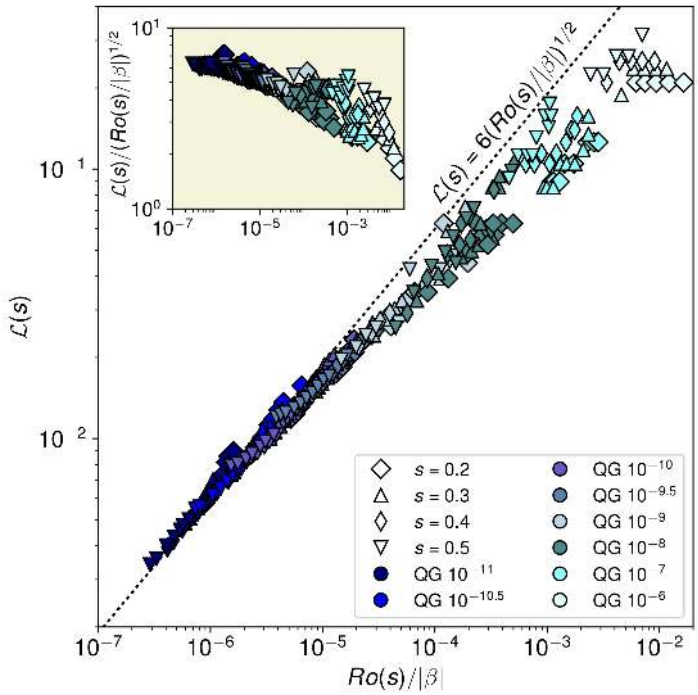

Figure 3: Convective lengthscale $\mathcal{L}(s)$ as a function of $Ro(s)/|\beta|$ obtained with the QG model at different radii. Marker colours correspond to Ekman numbers (with $Pr = 10^{-1}$ or 10^{-2}) and marker shapes to different radii. The inset shows the lengthscale compensated by the theoretical scaling as function of $Ro(s)/|\beta|$. The convective lengthscale corresponds to an azimuthal scale calculated from the peak of the power spectra of the radial kinetic energy at the radius s.

Extended Data Figure 4: Effect of the heating mode on the convective lengthscale

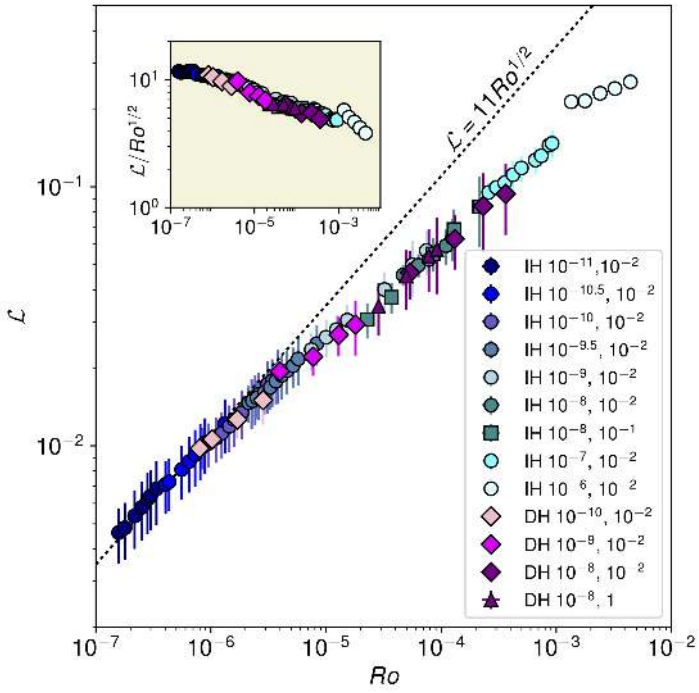

Figure 4: Convective lengthscale $\mathcal{L}$ as a function of Ro obtained with the QG model for internal heating (IH, same points as in Figure 4) and differential heating (DH) with an inner core of radius 0.35. The Ekman and Prandtl numbers are given in the legend. The convective scale is averaged in radius between $s = 0.1$ and 0.6 and the vertical bars give the standard deviation in this interval. The insets show the data compensated by the theoretical scaling as a function of Ro.

Extended Data Figure 5: Time series of the kinetic energy density for two representative simulations

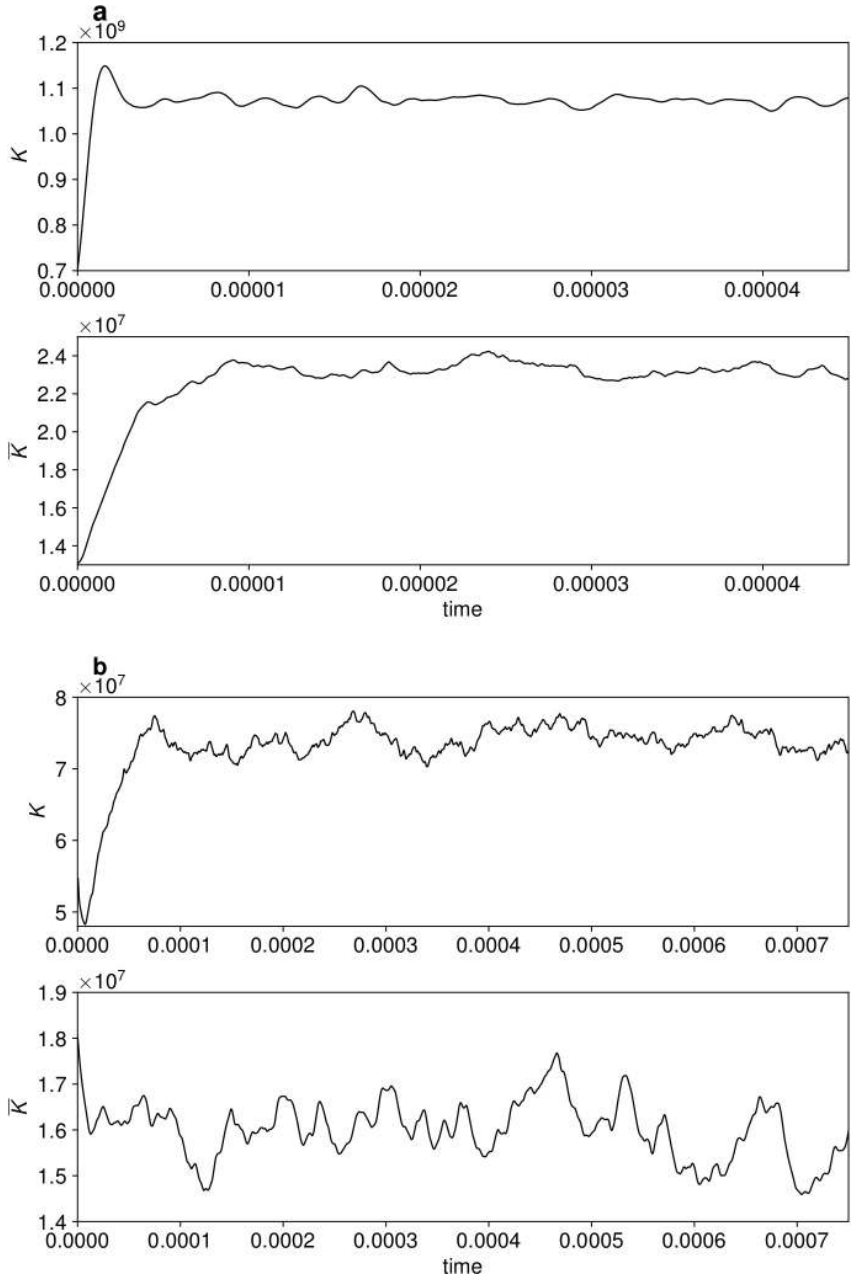

Figure 5: Time series of the kinetic energy density K and the kinetic energy density of the axisymmetric flow $\overline{K}$ for a) $Ek = 10^{-11}$, $Pr = 0.01$ and $Ra = 3.75 \times 10^{13}$ (QG model) and b) $Ek = 10^{-8}$, $Pr = 0.01$ and $Ra = 2 \times 10^{10}$ (3D model). The time is given in units of a viscous timescale.

Supplementary Information

Ek	Pr	Ra	Re	$\mathcal{L}$	$\mathcal{L}_r(s=0.5)$	(N_s, M)
10^{-6}	10^{-2}	6.000×10^7	1352 ± 171	0.213 ± 0.019	0.226 ± 0.102	$(600, 96)$
10^{-6}	10^{-2}	7.500×10^7	1778 ± 186	0.215 ± 0.025	0.235 ± 0.076	$(600, 96)$
10^{-6}	10^{-2}	1.050×10^8	2407 ± 215	0.230 ± 0.025	0.219 ± 0.084	$(600, 96)$
10^{-6}	10^{-2}	1.650×10^8	3239 ± 276	0.240 ± 0.029	0.244 ± 0.101	$(600, 128)$
10^{-6}	10^{-2}	2.850×10^8	4406 ± 334	0.254 ± 0.032	0.231 ± 0.082	$(600, 128)$
10^{-7}	10^{-2}	8.100×10^8	2588 ± 363	0.0852 ± 0.0213	0.121 ± 0.039	$(1000, 128)$
10^{-7}	10^{-2}	9.000×10^8	3015 ± 208	0.0875 ± 0.0231	0.125 ± 0.035	$(1000, 128)$
10^{-7}	10^{-2}	1.050×10^9	3569 ± 260	0.0915 ± 0.0259	0.126 ± 0.037	$(1000, 128)$
10^{-7}	10^{-2}	1.170×10^9	4204 ± 244	0.111 ± 0.015	0.127 ± 0.040	$(1000, 128)$
10^{-7}	10^{-2}	1.440×10^9	4989 ± 361	0.118 ± 0.013	0.133 ± 0.049	$(1000, 256)$
10^{-7}	10^{-2}	2.070×10^9	6588 ± 274	0.127 ± 0.015	0.150 ± 0.086	$(1200, 384)$
10^{-7}	10^{-2}	2.490×10^9	7411 ± 424	0.132 ± 0.012	0.168 ± 0.082	$(1200, 384)$
10^{-7}	10^{-2}	3.000×10^9	8659 ± 559	0.145 ± 0.013	0.188 ± 0.087	$(1200, 384)$
10^{-7}	10^{-2}	3.600×10^9	9214 ± 456	0.147 ± 0.018	0.195 ± 0.073	$(1200, 384)$
10^{-8}	10^{-2}	1.050×10^{10}	4678 ± 223	0.0457 ± 0.0043	0.0499 ± 0.0083	$(1600, 150)$
10^{-8}	10^{-2}	1.275×10^{10}	6359 ± 321	0.0498 ± 0.0051	0.0557 ± 0.0100	$(1600, 150)$
10^{-8}	10^{-2}	1.500×10^{10}	7826 ± 390	0.0524 ± 0.0055	0.0600 ± 0.0097	$(1600, 256)$
10^{-8}	10^{-2}	1.950×10^{10}	11030 ± 454	0.0592 ± 0.0091	0.0649 ± 0.0070	$(1600, 384)$
10^{-8}	10^{-2}	2.250×10^{10}	12561 ± 352	0.0634 ± 0.0117	0.0664 ± 0.0083	$(1600, 384)$
10^{-8}	10^{-1}	7.500×10^{10}	2279 ± 53	0.0307 ± 0.0048		$(2000, 400)$
10^{-8}	10^{-1}	1.200×10^{11}	3709 ± 68	0.0375 ± 0.0050		$(2000, 400)$
10^{-8}	10^{-1}	3.000×10^{11}	8485 ± 187	0.0551 ± 0.0081		$(2000, 500)$
10^{-8}	10^{-1}	4.500×10^{11}	12953 ± 287	0.0684 ± 0.0134		$(2000, 700)$
10^{-8}	10^{-1}	7.500×10^{11}	21623 ± 421	0.0838 ± 0.0253		$(2000, 1024)$
10^{-9}	10^{-2}	1.500×10^{11}	7458 ± 271	0.0235 ± 0.0039	0.0210 ± 0.0031	$(2000, 384)$
10^{-9}	10^{-2}	1.875×10^{11}	10026 ± 238	0.0262 ± 0.0042	0.0234 ± 0.0031	$(2000, 384)$
10^{-9}	10^{-2}	2.250×10^{11}	12346 ± 511	0.0281 ± 0.0039	0.0253 ± 0.0046	$(2000, 384)$
10^{-9}	10^{-2}	2.700×10^{11}	15300 ± 428	0.0306 ± 0.0043	0.0278 ± 0.0031	$(2000, 384)$
10^{-9}	10^{-2}	4.500×10^{11}	32274 ± 487	0.0401 ± 0.0066	0.0381 ± 0.0044	$(2000, 500)$
10^{-9}	10^{-2}	9.000×10^{11}	56251 ± 610	0.0499 ± 0.0123	0.0451 ± 0.0045	$(2000, 500)$
10^{-9}	10^{-2}	1.200×10^{12}	74423 ± 2222	0.0567 ± 0.0110	0.0501 ± 0.0065	$(2000, 512)$

Table 1: List of the input and output parameters for the simulations performed with the QG model. The azimuthal lengthscale $\mathcal{L}$ is averaged in radius between $s = 0.1$ and 0.6. The radial lengthscale $\mathcal{L}_r$ is given at radius $s = 0.5$. The last column gives the numerical resolution with N_s the number of grid points in radius and M the truncation order of the Fourier decomposition in azimuth.

Ek	Pr	Ra	Re	$\mathcal{L}$	$\mathcal{L}_r(s=0.5)$	(N_s, M)
$10^{-9.5}$	10^{-2}	4.575×10^{11}	6716 ± 165	0.0147 ± 0.0024	0.0116 ± 0.0011	$(2000, 512)$
$10^{-9.5}$	10^{-2}	4.725×10^{11}	7259 ± 205	0.0149 ± 0.0025	0.0122 ± 0.0012	$(2000, 512)$
$10^{-9.5}$	10^{-2}	4.950×10^{11}	7949 ± 204	0.0153 ± 0.0026	0.0130 ± 0.0011	$(2000, 512)$
$10^{-9.5}$	10^{-2}	5.445×10^{11}	9220 ± 205	0.0161 ± 0.0029	0.0139 ± 0.0013	$(2000, 512)$
$10^{-9.5}$	10^{-2}	6.000×10^{11}	10379 ± 221	0.0168 ± 0.0030	0.0146 ± 0.0017	$(2000, 512)$
$10^{-9.5}$	10^{-2}	6.600×10^{11}	11621 ± 265	0.0177 ± 0.0033	0.0150 ± 0.0013	$(2000, 600)$
$10^{-9.5}$	10^{-2}	7.350×10^{11}	13016 ± 235	0.0187 ± 0.0036	0.0159 ± 0.0016	$(2000, 600)$
$10^{-9.5}$	10^{-2}	8.100×10^{11}	14528 ± 288	0.0195 ± 0.0037	0.0166 ± 0.0015	$(2000, 600)$
$10^{-9.5}$	10^{-2}	9.000×10^{11}	16382 ± 285	0.0204 ± 0.0036	0.0173 ± 0.0020	$(2000, 650)$
$10^{-9.5}$	10^{-2}	9.900×10^{11}	18144 ± 341	0.0217 ± 0.0045	0.0178 ± 0.0015	$(2000, 650)$
$10^{-9.5}$	10^{-2}	1.350×10^{12}	26383 ± 745	0.0248 ± 0.0044	0.0207 ± 0.0028	$(2000, 650)$
10^{-10}	10^{-2}	1.725×10^{12}	8481 ± 129	0.00992 ± 0.0018	0.00771 ± 0.00062	$(1600, 512)$
10^{-10}	10^{-2}	1.800×10^{12}	9592 ± 152	0.0102 ± 0.0020	0.00841 ± 0.00075	$(1600, 512)$
10^{-10}	10^{-2}	1.950×10^{12}	11156 ± 168	0.0107 ± 0.0021	0.00906 ± 0.00075	$(1600, 512)$
10^{-10}	10^{-2}	2.100×10^{12}	12421 ± 136	0.0112 ± 0.0023	0.00944 ± 0.00072	$(1600, 512)$
10^{-10}	10^{-2}	2.400×10^{12}	14459 ± 182	0.0119 ± 0.0024	0.00999 ± 0.00097	$(1600, 512)$
10^{-10}	10^{-2}	2.700×10^{12}	15906 ± 173	0.0126 ± 0.0027	0.0105 ± 0.0008	$(2000, 512)$
10^{-10}	10^{-2}	3.150×10^{12}	18587 ± 214	0.0134 ± 0.0029	0.0110 ± 0.0013	$(2000, 512)$
10^{-10}	10^{-2}	3.900×10^{12}	22573 ± 279	0.0149 ± 0.0033	0.0121 ± 0.0011	$(3000, 700)$
10^{-10}	10^{-2}	4.200×10^{12}	24263 ± 324	0.0153 ± 0.0033	0.0124 ± 0.0015	$(3000, 700)$
10^{-10}	10^{-2}	4.500×10^{12}	26152 ± 289	0.0158 ± 0.0033	0.0126 ± 0.0014	$(3000, 700)$
10^{-10}	10^{-2}	5.250×10^{12}	31018 ± 316	0.0173 ± 0.0040	0.0136 ± 0.0012	$(3000, 900)$
10^{-10}	10^{-2}	5.700×10^{12}	34032 ± 534	0.0178 ± 0.0038	0.0137 ± 0.0011	$(3000, 900)$
10^{-10}	10^{-2}	6.300×10^{12}	38381 ± 672	0.0190 ± 0.0045	0.0146 ± 0.0016	$(3000, 1024)$
$10^{-10.5}$	10^{-2}	7.200×10^{12}	12779 ± 84	0.00709 ± 0.00161	0.00596 ± 0.00043	$(3500, 1024)$
$10^{-10.5}$	10^{-2}	7.500×10^{12}	13723 ± 113	0.00726 ± 0.00167	0.00621 ± 0.00077	$(3500, 1024)$
$10^{-10.5}$	10^{-2}	9.000×10^{12}	17621 ± 142	0.00810 ± 0.00192	0.00671 ± 0.00044	$(3500, 1024)$
$10^{-10.5}$	10^{-2}	1.050×10^{13}	20540 ± 145	0.00871 ± 0.00211	0.00717 ± 0.00045	$(3500, 1024)$
$10^{-10.5}$	10^{-2}	1.200×10^{13}	23086 ± 163	0.00924 ± 0.00228	0.00740 ± 0.00050	$(3500, 1024)$
$10^{-10.5}$	10^{-2}	1.350×10^{13}	25577 ± 202	0.00976 ± 0.00240	0.00779 ± 0.00055	$(3500, 1024)$
$10^{-10.5}$	10^{-2}	1.500×10^{13}	28174 ± 256	0.0103 ± 0.0025	0.00795 ± 0.00057	$(3500, 1024)$
$10^{-10.5}$	10^{-2}	2.250×10^{13}	41907 ± 290	0.0122 ± 0.0029	0.00945 ± 0.00094	$(3500, 1024)$
10^{-11}	10^{-2}	2.700×10^{13}	15800 ± 83	0.00462 ± 0.00112	0.00403 ± 0.00022	$(2400, 950)$
10^{-11}	10^{-2}	2.850×10^{13}	17897 ± 91	0.00482 ± 0.00120	0.00427 ± 0.00018	$(2400, 1024)$
10^{-11}	10^{-2}	3.300×10^{13}	21754 ± 99	0.00536 ± 0.00137	0.00455 ± 0.00027	$(4000, 1100)$
10^{-11}	10^{-2}	3.750×10^{13}	25243 ± 127	0.00579 ± 0.00149	0.00485 ± 0.00016	$(4000, 1536)$
10^{-11}	10^{-2}	4.200×10^{13}	28140 ± 108	0.00622 ± 0.00166	0.00496 ± 0.00026	$(4000, 2048)$
10^{-11}	10^{-2}	4.500×10^{13}	29846 ± 85	0.00639 ± 0.00168	0.00514 ± 0.00019	$(4000, 2048)$
10^{-11}	10^{-2}	5.250×10^{13}	33657 ± 211	0.00682 ± 0.00189	0.00537 ± 0.00025	$(4000, 2048)$

Table 1: Continued.

Ek	Pr	Ra	Re	$\mathcal{L}$	(N_r, L, M)
10^{-6}	10^{-2}	6.02×10^7	1160 ± 148	0.268 ± 0.029	$(560, 150, 127)$
10^{-6}	10^{-2}	1.00×10^8	2050 ± 139	0.315 ± 0.037	$(560, 150, 127)$
10^{-6}	10^{-2}	2.00×10^8	3370 ± 177	0.376 ± 0.048	$(560, 150, 127)$
10^{-7}	10^{-2}	7.00×10^8	1470 ± 201	0.0943 ± 0.0136	$(1152, 199, 159)$
10^{-7}	10^{-2}	1.10×10^9	3340 ± 190	0.115 ± 0.0089	$(1152, 199, 159)$
10^{-7}	10^{-2}	1.25×10^9	3800 ± 213	0.119 ± 0.0079	$(1152, 199, 159)$
3×10^{-8}	10^{-2}	3.00×10^9	2897 ± 150	0.0648 ± 0.0035	$(1568, 277, 255)$
3×10^{-8}	10^{-2}	4.00×10^9	3967 ± 85	0.0719 ± 0.0036	$(1568, 277, 255)$
3×10^{-8}	10^{-2}	5.10×10^9	4600 ± 96	0.0754 ± 0.0051	$(1568, 277, 255)$
10^{-8}	10^{-2}	1.50×10^{10}	4780 ± 75	0.0492 ± 0.0056	$(2016, 351, 319)$
10^{-8}	10^{-2}	2.00×10^{10}	5550 ± 70	0.0525 ± 0.0061	$(2016, 351, 319)$
10^{-8}	10^{-2}	2.50×10^{10}	6100 ± 82	0.0560 ± 0.0079	$(2016, 351, 319)$

Table 2: List of the input and output parameters for the simulations performed with the 3D model. The azimuthal lengthscale $\mathcal{L}$ is averaged in radius between $s = 0.1$ and 0.6. The last column gives the numerical resolution with N_r the number of grid points in radius, L and M the truncation degree and order of the spherical harmonics.

Ek	Pr	Ra	Re	$\mathcal{L}$	(N_s, M)
10^{-8}	1	1.780×10^{11}	2864 ± 31	0.0346 ± 0.0079	$(4000, 600)$
10^{-8}	1	2.670×10^{11}	4979 ± 76	0.0452 ± 0.0118	$(4000, 600)$
10^{-8}	1	3.560×10^{11}	7825 ± 244	0.0540 ± 0.0147	$(4000, 800)$
10^{-8}	1	4.450×10^{11}	9151 ± 365	0.0573 ± 0.0188	$(4000, 800)$
10^{-8}	10^{-2}	1.780×10^{9}	5372 ± 149	0.0467 ± 0.0100	$(2000, 200)$
10^{-8}	10^{-2}	3.560×10^{9}	13161 ± 423	0.0629 ± 0.0151	$(2000, 300)$
10^{-8}	10^{-2}	6.675×10^{9}	23267 ± 592	0.0843 ± 0.0286	$(2000, 300)$
10^{-8}	10^{-2}	1.113×10^{10}	36404 ± 620	0.0939 ± 0.0288	$(2500, 384)$
10^{-9}	10^{-2}	1.780×10^{10}	3967 ± 231	0.0194 ± 0.0016	$(2000, 384)$
10^{-9}	10^{-2}	2.225×10^{10}	7726 ± 129	0.0221 ± 0.0034	$(2000, 384)$
10^{-9}	10^{-2}	3.115×10^{10}	12884 ± 180	0.0268 ± 0.0047	$(2000, 384)$
10^{-9}	10^{-2}	4.005×10^{10}	18033 ± 188	0.0293 ± 0.0070	$(2000, 384)$
10^{-10}	10^{-2}	2.670×10^{11}	7998 ± 53	0.0098 ± 0.0003	$(3000, 700)$
10^{-10}	10^{-2}	3.115×10^{11}	10210 ± 95	0.0106 ± 0.0005	$(3000, 700)$
10^{-10}	10^{-2}	4.450×10^{11}	16947 ± 112	0.0126 ± 0.0019	$(3000, 700)$
10^{-10}	10^{-2}	6.675×10^{11}	28376 ± 165	0.0150 ± 0.0029	$(3000, 700)$

Table 3: List of the input and output parameters for the simulations performed with the QG model with differential heating and an inner core of radius $R_i = 0.35$. The azimuthal lengthscale $\mathcal{L}$ is averaged in radius between $s = 0.35$ and 0.6. The last column gives the numerical resolution with N_s the number of grid points in radius and M the truncation order of the Fourier decomposition in azimuth.